Applied Surface Science 487 (2019) 981–989

Contents lists available at ScienceDirect

Applied Surface Science

journal homepage: www.elsevier.com/locate/apsusc

Full length article

Effect of oxygen incorporation in amorphous molybdenum sulfide on electrochemical hydrogen evolution

Seokhee Shin, Zhenyu Jin, So-Yeon Ham, Suhyun Lee, Da-Som Shin, Yo-Sep Min*

Department of Chemical Engineering, Konkuk University, 120 Neungdong-Ro, Gwangjin-Gu, Seoul 05029, Republic of Korea

ARTICLE INFO

Keywords:
Electrochemical hydrogen evolution
Amorphous
Molybdenum sulfide
Oxygen incorporation
Molybdenum oxysulfide
Molybdenum oxidation state

ABSTRACT

Amorphous molybdenum sulfide (MoS_x) has attracted great attention as an alternative catalyst of platinum for electrochemical hydrogen evolution reaction (HER). In order to investigate the effect of oxygen incorporation in the MoS_x catalyst, oxygen-incorporated MoO_xS_y catalysts with various oxygen contents were prepared on carbon fiber papers (CFPs) by chemical bath deposition. The oxygen content and chemical states of MoO_xS_y catalysts were controlled by adjusting the reducing agent concentration of $Na_2S_2O_4$ in order to reveal the relation between chemical states and HER performance. Compared to oxygen-free MoS_x catalysts, the oxygen-incorporated MoO_xS_y catalysts exhibit more excellent activity for HER. One of the MoO_xS_y catalysts requires an overpotential of 164 mV to reach a cathodic current density of 10 mA/cm^2 with a Tafel slope of 43 mV/dec representing the Volmer-Heyrovsky mechanism. The high performance is attributed to enhanced activity and/or higher electrical conductivity due to the presence of Mo^{5+} state in the MoO_xS_y catalysts.

1. Introduction

In order to reduce consumption of fossil fuels causing environmental pollution and global warming, various approaches to utilize solar energy have been extensively studied in academia and industry. In photovoltaics, solar energy is directly converted to electrical energy in solar cells specially designed to maximize the photon-to-electron conversion efficiency. However, since the sunlight changes with the rotation and revolution of the earth, the electrical energy converted from the sun should be stored somewhere for use in the dark.

Photoelectrochemical (PEC) water splitting can be a solution for the solar energy conversion and storage in an environmentally friendly and sustainable manner because the solar energy is converted to the chemical energy of hydrogen molecules [1]. For the PEC water splitting, catalysts such as platinum group metals (PGMs) are required to reduce the overpotentials for electrochemically splitting water molecules to hydrogen and oxygen gases. Even though the PGM catalysts have high activities for both hydrogen and oxygen evolution reactions (HER and OER), they should be replaced by inexpensive catalysts for practical applications.

Recently, transition metal sulfides [2,3], phosphides [4], nitrides [5] and carbides [6] have been extensively explored as an alternative HER catalyst to replace the PGMs. Especially, MoS_2-based catalysts have attracted great attention owing to their high activity. Crystalline MoS_2, such as 2H-MoS_2, exhibits a high activity on the edge sites of the layered structure, but the basal planes are inactive to the HER [7]. Therefore, vertically aligned MoS_2 has been studied in order to maximize the active sites by vertically exposing the edge of MoS_2 [8–10]. Another strategy for highly active MoS_2 catalysts is activation of the inactive basal plane by creating defects such as S-vacancies or by doping heteroatoms on the basal MoS_2 [11–19]. It was revealed that S-vacancy sites, as well as edge sites, are also catalytically active for HER. MoS_2 with S-vacancies exhibits more excellent HER performance comparing to MoS_2 without S-vacancies. Doped-heteroatoms into MoS_2 basal plane also enhance the HER catalytic activity [12,20,21]. Recently, amorphous MoS_x also has attracted great attention as an excellent HER catalyst, since the structural heterogeneity of the amorphous MoS_x provides active sites as in the edge of the crystalline MoS_2 [22–30]. In addition, the electrical conductivity of catalyst is one of the important factors for high HER performance. Xile Hu group reported that MoS_3 catalysts with high conductivity have a smaller value of Tafel slope than those with low conductivity [31]. Therefore, the limited HER performance of the less conductive catalysts can be improved by using an electrically conductive substrate or increasing the conductivity of catalysts.

Introducing dopants into catalysts is a frequently used strategy to tune the electronic structure of the materials [32]. The doping process may result in several positive effects on the catalysts: tuning an

* Corresponding author.
E-mail address: ysmin@konkuk.ac.kr (Y.-S. Min).

https://doi.org/10.1016/j.apsusc.2019.05.188
Received 12 March 2019; Received in revised form 27 April 2019; Accepted 16 May 2019
Available online 17 May 2019
0169-4332/

adsorption free energy of hydrogen (ΔG_H) into 0 eV [24,33–38], creating more active sites [20,33], and/or increasing an electrical conductivity [33,38,39]. Vertically aligned MoS_2 catalysts doped with transition metals (e.g., Fe, Co, Ni, or Cu) possess more active edge sites of which ΔG_H is close to 0 eV [34]. The improvement of the HER activity by doping was also reported for Fe, Co, or Ni-doped amorphous MoS_x catalysts [24]. Pan and co-workers reported that half-filled intermediate energy bands of Co-doped MoS_2 improve the catalytic activity of Co-MoS_2 by lowering the energy barriers for charge transfer to proton [33]. Lau and co-workers exhibited that Co adatoms on MoS_2 basal plane reduce the hydrogen adsorption free energy on neighbor S sites of Co atom [37]. Other 3d transition metal dopants like Zn [38], Mn [40], V [39] also facilitate the HER through similar ways as mentioned above. In addition, Deng and co-workers reported that Pt atoms, which replace Mo atoms of MoS_2, produce unsaturated sulfur atoms at the sites facing the doped Pt atoms, and the electronic structure of the coordinatively unsaturated sulfur is similar to that of the MoS_2 edge sites [20]. Moreover, non-metallic dopants like Se [41], O [42–47], P [48], Cl [36] and N [35] also improve the catalytic activity of MoS_2.

For the oxygen doping, there are several reports that oxygen atoms in O-incorporated MoS_2 (MoO_xS_y) catalysts improve the HER performances by increasing the intrinsic electrical conductivity as well as forming more active sites for HER [42,44–47,49]. For example, the resistivity (0.033 Ω·cm) of MoO_xS_y on reduced graphene oxide (rGO) is much lower than that (0.25 Ω·cm) of MoS_2/rGO [45]. Xie and co-workers reported that the presence of oxygen in MoO_xS_y increases a degree of disorder which results in more active sites for HER [42]. They claimed that the proper oxygen contents in MoO_xS_y improve the electrical conductivity by reducing the band gap of MoO_xS_y, but excessive incorporation of oxygen atoms causes degradation of the HER performance by restricting the interdomain electron transport [42].

Oxygen incorporation in amorphous molybdenum sulfide catalysts is a significant approach to improve HER performance, but no studies have been reported on the effect of the oxygen incorporation for the amorphous phase of MoS_x catalysts. In this study, molybdenum oxysulfide (MoO_xS_y) with various oxygen contents were synthesized by a facile chemical bath deposition (CBD) and the effect of oxygen incorporation on the HER activity was investigated in order to unveil the influence of chemical states of Mo and S ions on the catalytic activity.

2. Experimental

2.1. Materials synthesis

For syntheses of MoO_xS_y catalysts by the CBD method, ammonium heptamolybdate ($(NH_4)_6Mo_7O_{24}{\cdot}4H_2O$, 99.0%, Samchun Chemical Co.), thioacetamide (CH_3CSNH_2, 99.0%, Sigma-Aldrich), ammonium hydroxide (NH_4OH, 28–30%, Samchun Chemical Co.) and sodium dithionite (also known as sodium hydrosulfite, $Na_2S_2O_4$, 85%, Alfa Aesar) were purchased and used without further purification. Aqueous solutions of $(NH_4)_6Mo_7O_{24}{\cdot}4H_2O$ (10 mM, 10 mL) and CH_3CSNH_2 (1 M, 15 mL) were mixed in a vial bottle. Subsequently, an aqueous solution of NH_4OH (14.8 M, 15 mL) was added to the mixture. As a reducing agent to control the oxygen content, aqueous solutions of $Na_2S_2O_4$ (10 mL) with various concentrations (7.6, 38, 380, and 760 mM) were prepared, and each $Na_2S_2O_4$ solution was added to the previously prepared solutions of precursors. Therefore, the volumes of the resulting precursor solutions were around 50 mL for each CBD solution. Carbon fiber papers (Toray, TGP-H-120), on which catalysts would be deposited, were placed in each precursor solution, and then the vial bottles were maintained at 90 °C for 30 min without any stirring for the CBD of MoO_xS_y catalysts on CFPs. After the deposition, the vial bottles were cooled down to room temperature for 5 h and MoO_xS_y-coated CFPs (MoO_xS_y/CFPs) were taken out from the solution. The MoO_xS_y/CFPs were washed in turn with deionized water, ethanol, and acetone, and then dried in air.

2.2. Materials characterization

The X-ray diffraction (XRD) patterns were obtained at an incident angle of 1° using a Rigaku SmartLab diffractometer with Cu Kα emission. Field-emission scanning electron microscope (FE-SEM) images were taken using a Hitachi SU8010 without any coating of metal. X-ray photoelectron spectroscopic (XPS) spectra were collected from a PHI 5000 Versaprobe (ULVAC PHI) using monochromatic Al Kα emission. Binding energies were calibrated using C 1s peak (284.8 eV) of the adventitious carbon as an internal standard. To avoid misinterpretation due to surface contamination and oxidation in air, the surface of each specimen was cleaned by bombarding Ar^+ ions (2 keV) for 10 s before obtaining the XPS spectra. Raman spectroscopy (Alpha 500R, Witech) was also performed to characterize the MoO_xS_y catalyst using a 532 nm laser excitation.

2.3. Electrochemical hydrogen evolution

Electrochemical characterization of the prepared catalysts for HER was performed by a three electrodes configuration using a Biologic (SP-150) potentiostat. MoO_xS_y/CFP, carbon rod, and K_2SO_4 saturated Hg/Hg_2SO_4 were used as working, counter and reference electrode, respectively. All experiments were carried out in 0.5 M H_2SO_4 solution at room temperature. Before the evaluation of HER performance, the reference electrode was calibrated by using two Pt wires as the working and counter electrodes in 0.5 M H_2SO_4 solution. The electrochemical potential difference between the reversible hydrogen electrode (RHE) and the reference electrode is given by E(RHE) = E(Hg/Hg_2SO_4) + 0.705 V. The polarization curves of HER were measured using linear sweep voltammetry (LSV) at a potential range of + 0.1 V to − 0.4 V vs RHE. Series resistances of the electrochemical cells were determined by electrochemical impedance spectroscopy (EIS) performed at open circuit potential from 200 kHz to 50 mHz, using an ac amplitude of 25 mV. The polarization curves were corrected for ohmic potential drop (*iR*) losses using the series resistances obtained from the EIS. In order to estimate the electrochemically active surface area (ECSA) of catalysts, the double-layer capacitance (C_{dl}) of MoO_xS_y/CFPs were determined by cyclic voltammetry in a potential range from 0.10 to 0.20 V vs RHE with various scan rates of 20, 40, 60, 80 and 100 mV/s.

3. Results and discussion

Molybdenum oxysulfide (MoO_xS_y) catalysts were directly synthesized on carbon fiber papers (CFPs) at 90 °C by using the CBD precursor solutions with various concentrations of $Na_2S_2O_4$. Sodium dithionite is well known as a reducing agent for various chemical reactions [50]. Because its dithionite anion has a weak S—S bond, it is in equilibrium with the radical anion, $S_2O_4^{2-} \rightleftharpoons 2\,SO_2^-$ [51]. Therefore sodium dithionite is a strong and rapid reducing agent. During the CBD reaction, the oxidation state of sulfur in the dithionite anion is oxidized from S^{3+} of $S_2O_4^{2-}$ to S^{4+} of HSO_3^- by releasing two electrons (see Eq. (1)). These electrons are accepted by molybdate (MoO_4^{2-}) ions to reduce Mo^{6+} to Mo^{5+} or Mo^{4+} ions. Note that even though ammonium heptamolybdate was used as a Mo precursor, molybdates are present as the monomeric MoO_4^{2-} ion in alkaline and neutral solutions [52]. The sulfide ions for the synthesis of MoO_xS_y catalyst are formed from the reaction between thioacetamide and hydroxide ion in the aqueous solution (see Eq. (2)) [53]. Therefore it is expected that the oxygen content of MoO_xS_y catalyst depends on the concentration of sodium dithionite.

$$S_2O_4^{2-} + 2H_2O \rightarrow 2HSO_3^- + 2e^- + 2H^+ \quad (1)$$

$$CH_3C(=S)NH_2 + OH^- + H_2O \rightarrow CH_3C(=O)NH_2 + S^{2-} + H_3O^+ \quad (2)$$

For convenience, we denote these catalysts as RA_0 (0 mM), RA_1

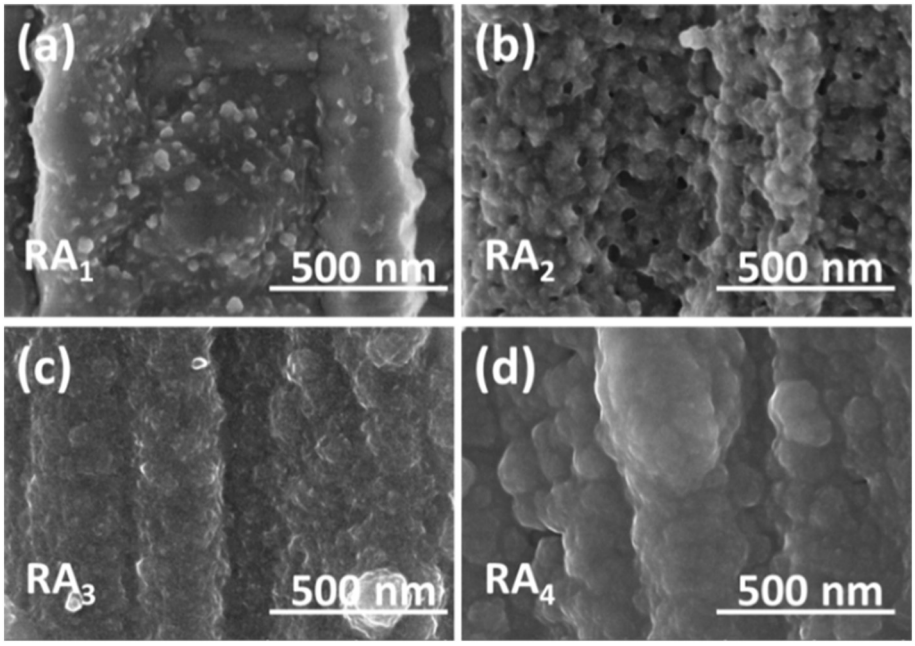

Fig. 1. FE-SEM images of MoO_xS_y/CFP catalysts.

(7.6 mM), RA_2 (38 mM), RA_3 (380 mM) and RA_4 (760 mM) of which the subscript number increases with the concentration of the reducing agent ($Na_2S_2O_4$) in the CBD precursor solution. The synthesized MoO_xS_y catalysts are amorphous as shown in the X-ray diffraction patterns (Fig. S1) in which there is no peak from MoO_xS_y but several peaks from the graphitic structure of the CFP substrate.

The surface morphology of the heterogeneous catalysts such as MoO_xS_y/CFPs is one of the crucial factors affecting electrocatalytic performances because electrocatalytic reactions occur on the surface of the catalyst. Fig. 1 shows that the MoO_xS_y catalysts (RA_2, RA_3, and RA_4) synthesized above the reducing agent concentration of 38 mM (RA_2) cover completely the CFP in Fig. 1(b–d). However, by comparing the SEM images of RA_1 (Fig. 1a) and bare CFP (Fig. S2), it can be seen that the MoO_xS_y catalyst (RA_1) deposited with a low concentration of 7.6 mM does not completely cover the CFP. Moreover, the CBD process performed without the reducing agent (RA_0) does not cause significant growth of the catalyst, as revealed by the noisy XPS spectra of Mo and S in Fig. S3.

XPS analyses were performed to investigate the composition and the chemical states of each MoO_xS_y catalyst. The stoichiometric values of x and y of MoO_xS_y catalysts are listed in Table 1. The ratio of chalcogens (S and O) to molybdenum atom is deviated from 2 and scattered in the range of 2.75 to 3.08, which reveals that the sum of the stoichiometric values is around three (i.e., $x + y \approx 3$) and the chemical states of Mo^{4+} and S^{2-} may be mixed with other states (Mo^{6+}, Mo^{5+} and/or S_2^{2-}). In Fig. 2, as the concentration of $Na_2S_2O_4$ in the precursor solution increases to 380 mM, the S content increases but the O content decreases, since $Na_2S_2O_4$ plays the role of a reducing agent. However, the S content nearly saturates at 760 mM with a higher O content.

The incorporation of oxygen was also confirmed by Raman spectroscopy. In the representative Raman spectrum (Fig. 3) of MoO_xS_y/CFP

Table 1
Stoichiometric values of MoO_xS_y catalysts.

Catalyst	x (O/Mo)	y (S/Mo)	x + y
RA_1	1.95	0.81	2.75
RA_2	1.90	1.01	2.91
RA_3	1.49	1.38	2.87
RA_4	1.75	1.33	3.08

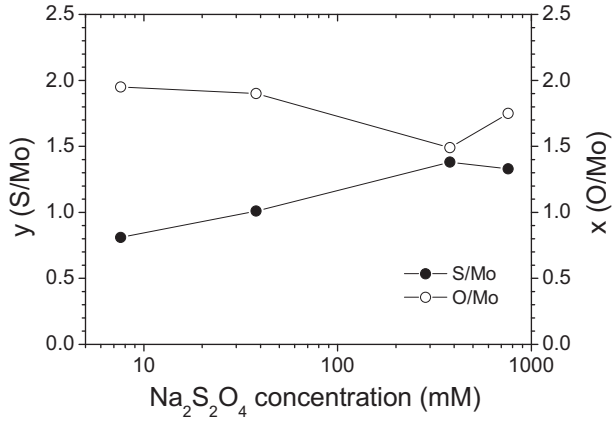

Fig. 2. Stoichiometric values of oxygen (x) and sulfur (y) of MoO_xS_y/CFP catalysts against the concentration of the reducing agent ($Na_2S_2O_4$).

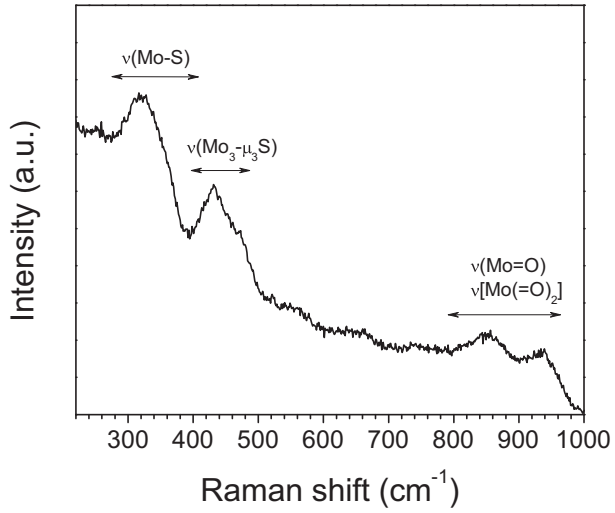

Fig. 3. Representative Raman spectrum of MoO_xS_y/CFP catalysts (RA_3).

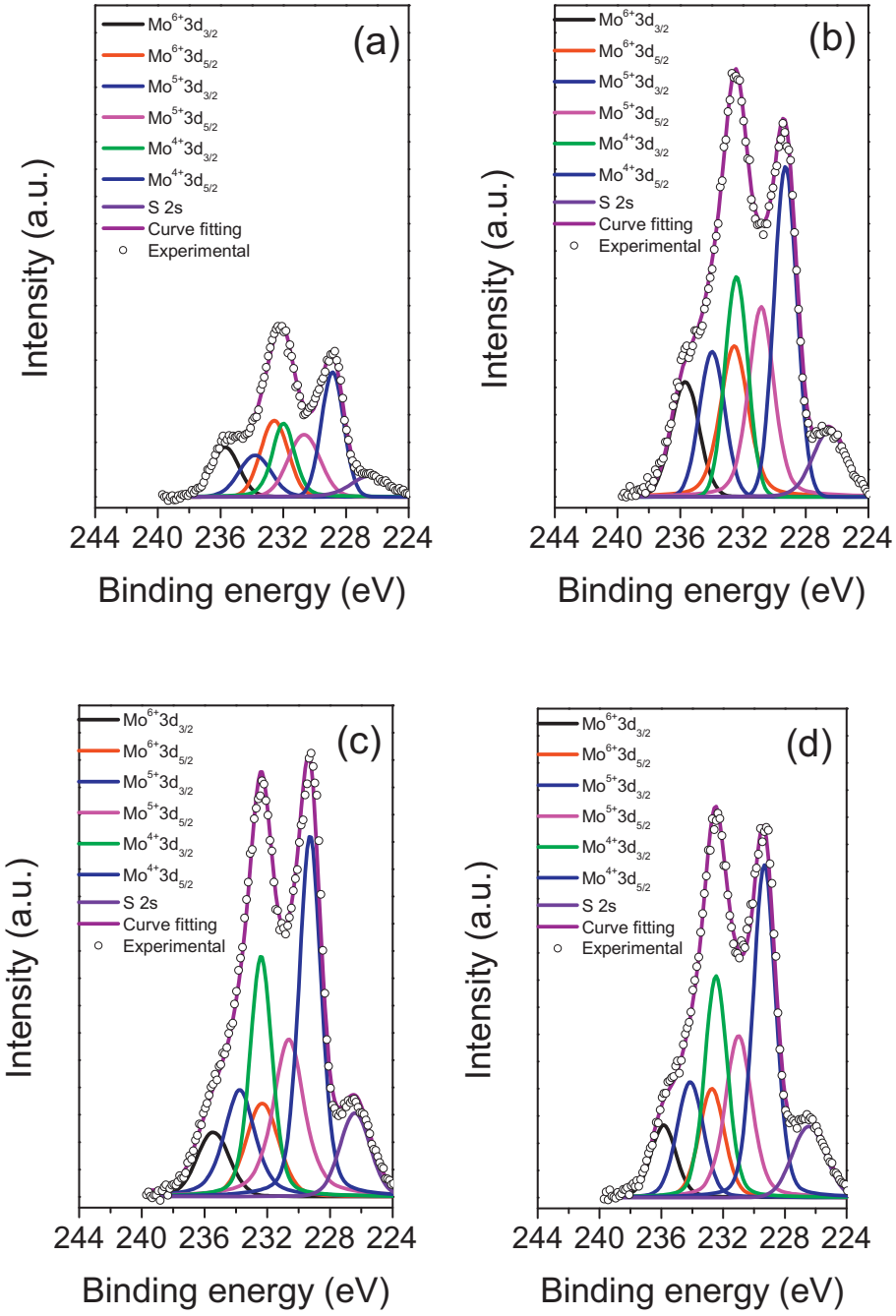

Fig. 4. XPS spectra of Mo 3d core electrons of MoO_xS_y/CFP catalysts: RA_1 (a), RA_2 (b), RA_3 (c) and RA_4 (d).

(RA_3) of which MoO_xS_y completely covers the CFP substrate, molybdenum sulfide bonds were found at ν(Mo−S) of 283–385 cm^{-1} and the $\nu(Mo_3\text{-}\mu_3S)$ vibration was observed in the 395–478 cm^{-1} region. Furthermore, the bands of Mo=O vibration were clearly observed in a wide range of 800–960 cm^{-1}. These Raman signatures are in good agreement with the previous report by Tran et al. [53].

In order to analyze the chemical states of Mo and S atoms, the XPS spectra of Mo 3d and S 2p were deconvoluted by fitting the experimental data with plausible peaks as shown in Figs. 4 and 5. All binding energies were calibrated with the carbon 1 s peak at 284.8 eV. For the Mo 3d spectra, the peaks were deconvoluted into binding energies of three doublets ($3d_{3/2}$ and $3d_{5/2}$) of Mo^{6+}, Mo^{5+}, Mo^{4+} and a singlet of S 2s state. All 3d doublets were fitted under two constraints: the area ratio of 2:3 and the binding energy difference (3.13 eV) between $3d_{3/2}$ and $3d_{5/2}$ peaks. In Fig. 4 and Table S1, as the oxidation number of molybdenum increases in the ascending order of Mo^{4+}, Mo^{5+} and Mo^{6+} ions, the characteristic doublets ($3d_{3/2}$ and $3d_{5/2}$) of molybdenum atoms are found at higher binding energies which coincide with the previous report [54]. In Fig. 6(a), the ratio of Mo^{4+} to total molybdenum ions (Mo^{4+} + Mo^{5+} + Mo^{6+}) increases with the concentration of reducing agent, but the ratio of Mo^{6+} decreases with the concentration of reducing agent, because $Na_2S_2O_4$ reduces the Mo^{6+} ions in form of MoO_4^{2-} into the Mo^{4+} by producing molybdenum sulfide. However, the ratio of Mo^{5+} ions shows a small variation in the range of 0.29 to 0.33, not depending on the concentration of the reducing agent.

For the spectra of S 2p, the experimental peaks of S 2p were also deconvoluted to the doublets of $2p_{1/2}$ and $2p_{3/2}$ with the area ratio of 1:2 and the binding energy difference of 1.18 eV. The deconvoluted S 2p spectra consist of three doublets from divalent sulfur (S^{2-}),

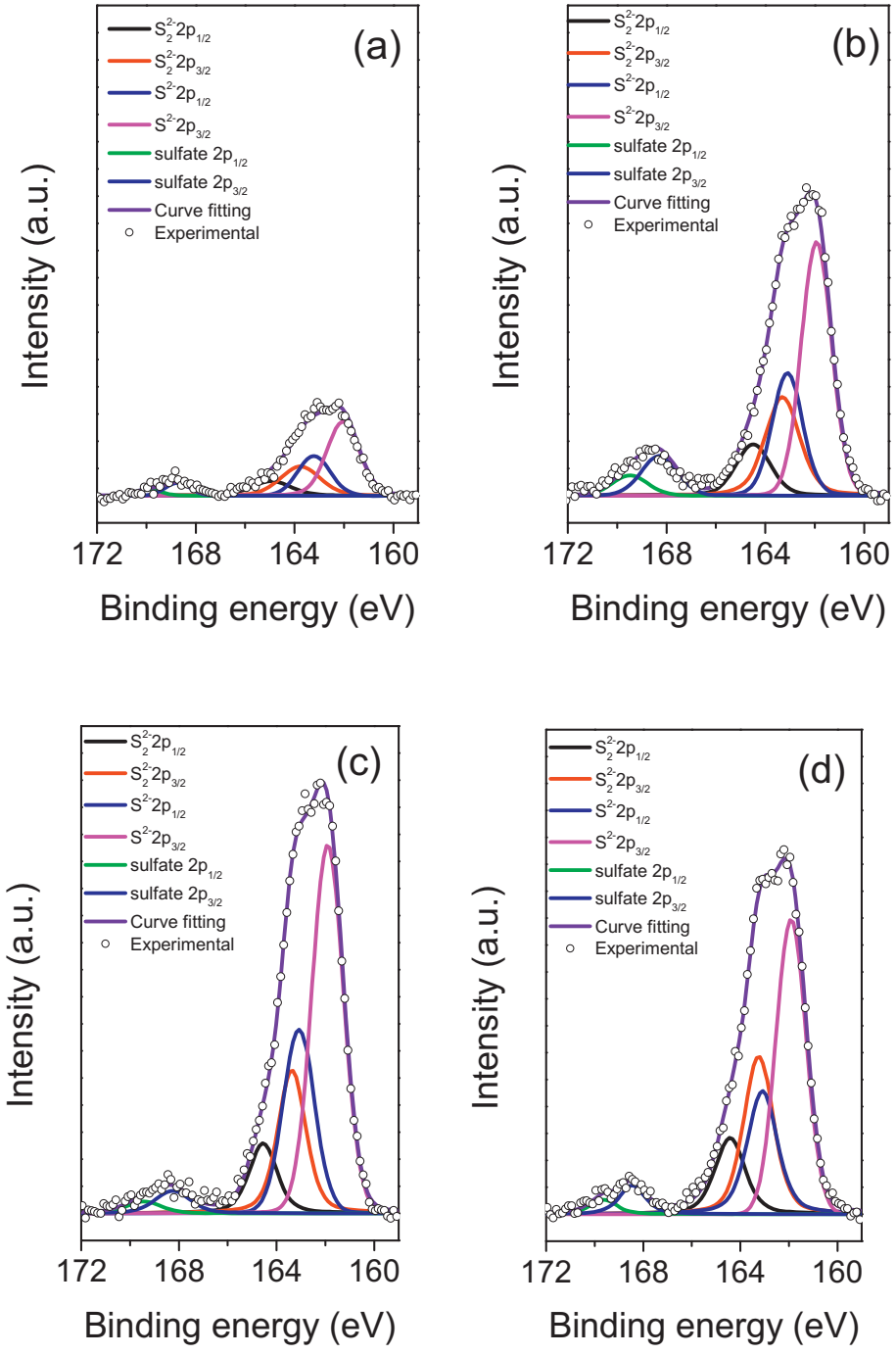

Fig. 5. XPS spectra of S 2p core electrons of MoO_xS_y/CFP catalysts: RA_1 (a), RA_2 (b), RA_3 (c) and RA_4 (d).

monovalent sulfur (S_2^{2-}) and sulfate (S^{6+}) in Fig. 5(a–d) and Table S1. Two doublets deconvoluted in the range of 160 to 166 eV were assigned to the doublets of S^{2-} and S_2^{2-} where the doublet of S_2^{2-} has higher binding energy than that of S^{2-}. As shown in Fig. 6(b), the content of S^{2-} ions is about twice the content of S_2^{2-} ions. The small doublets in the range of 167 to 171 eV are associated with S^{6+} from sulfate (SO_4^{2-}) ion, indicating that the surface of the synthesized catalysts was oxidized by exposure in the air when the catalysts were dried in air.

In order to investigate catalytic activity of the amorphous MoO_xS_y/CFP catalysts for HER, *iR*-corrected polarization curves were obtained using a standard three-electrode setup in a 0.5 M H_2SO_4 solution as shown with solid lines in Fig. 7. The exchange current density (j_0), Tafel slope (b), and the overpotential (η_{10}) required to reach the cathodic current density of 10 mA/cm^2 are generally used to comparatively evaluate catalytic activity of HER catalysts. These values of the MoO_xS_y/CFP catalysts are listed in Table 2. Bare CFP without any catalyst has no catalytic effect for HER. Furthermore, the activity of the catalyst R_0 synthesized without any $Na_2S_2O_4$ is so poor that the cathodic current density of R_0 does not reach 10 mA/cm^2 in the potential range of 0 to −0.3 V vs RHE (η_{10} = 500 mV for R_0 in Table 2). However, as the concentration of $Na_2S_2O_4$ increases, the catalysts exhibit smaller overpotentials of η_{10} in the order of RA_0 (500 mV), RA_1 (216 mV), RA_2 (184 mV), RA_3 (166 mV) and RA_4 (164 mV). The reason for the remarkably poor catalytic activity of the RA_0 and RA_1 catalysts is due to partial or incomplete coverage (i.e. negligible or small loading) of MoO_xS_y on the CFP, as demonstrated in the SEM image and

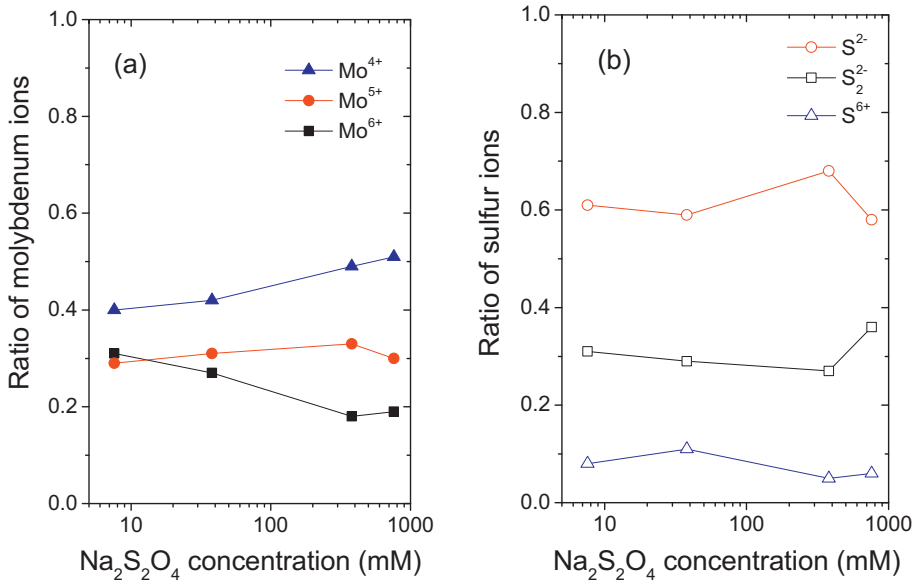

Fig. 6. (a) Ratio of each Mo ion to total Mo ions; (b) ratio of each S ion to total S ions.

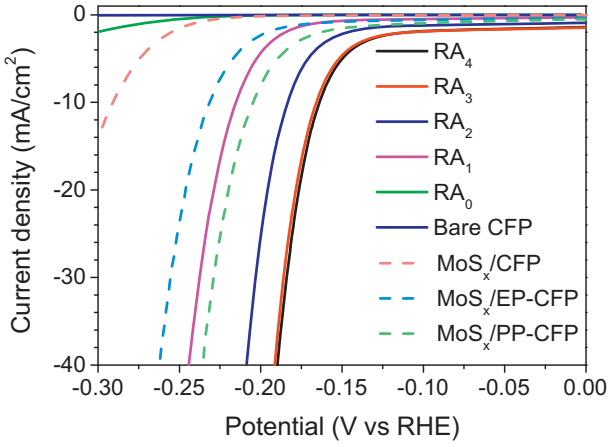

Fig. 7. *iR*-corrected polarization curves of MoO_xS_y/CFPs (a) prepared by CBD and MoS_x/CFPs (a) reported in our previous work (Ref. [58]).

Table 2
Electrochemical characteristics of MoO_xS_y (this work) and MoS_x (our previous work in Ref. [58] catalysts.

Catalyst	η_{10} mV	*b* mV/dec	j_0 μA/cm^2	C_{dl} mF/cm^2
RA_0	500	54	0.012	0.04
RA_1	216	43	0.094	6.55
RA_2	184	42	0.400	30.1
RA_3	166	43	1.640	68.1
RA_4	164	43	1.560	66.6
MoS_x/CFP	290	46	0.006	0.17
MoS_x/EPCFP	231	49	0.178	1.68
MoS_x/PPCFP	205	50	0.863	4.13

XPS spectra (Figs. 1(a), S2 and S3). The coverage of MoO_xS_y catalysts gradually increases with the concentration of the reducing agent, and MoO_xS_y is completely covered on the CFP substrate at the concentration of 38 mM (RA_2) as shown in Figs. 1 and S2. Even though the catalysts of RA_2, RA_3, and RA_4 have the complete coverage on the CFP, the η_{10} value of RA_2 is severely different from those of RA_3 and RA_4. This is due to the difference in chemical composition and chemical state of the catalysts.

Because the electrochemically active surface area (ECSA) of the catalyst is directly related to the HER performance, the electric double layer capacitances (C_{dl}) were determined using cyclic voltammetry (CV) performed in the range of 0.10 to 0.20 V vs RHE at various scan rates (ν) of 20, 40, 60, 80 and 100 mV/s (Fig. S4). Half ($\Delta j/2$) of the difference in anodic (j_a) and cathodic (j_c) current densities is plotted against the scan rate in Fig. S5, since the double layer capacitance can be expressed as $C_{dl} = \Delta j / 2\nu$. From the slopes of each plot in Fig. S5, the C_{dl} values were determined and listed in Table 2. It should be noted that the ECSA is proportional to the C_{dl} value. The C_{dl} values of RA_0, RA_1, RA_2, RA_3, and RA_4 catalysts are 0.04, 6.55, 30.1, 68.1 and 66.6 mF/cm^2, respectively, indicating that ECSA becomes larger with the concentration of the reducing agent.

The exchange current density (j_0) and Tafel slope (*b*) can be obtained from the Tafel plot where the overpotential (η) is plotted against cathodic current density (*j*) with the Tafel equation of $\eta = a + b\log j$. The j_0 value of HER reflects how fast hydrogen gas evolves on the catalyst in equilibrium (i.e., at zero overpotential). The j_0 value is determined by extracting the intercept in the log *j* axis of the Tafel plot (Fig. 8). The higher the j_0 value of the MoO_xS_y/CFP is, the faster the HER on the catalyst is. In Table 2, the j_0 values of RA_3 (1.64 μA/cm^2) and RA_4 (1.56 μA/cm^2) catalysts are much higher than the other catalysts (0.0123–0.4 μA/cm^2). However, the simple comparison of the j_0 values can be unfair to evaluate the intrinsic activity of the MoO_xS_y/

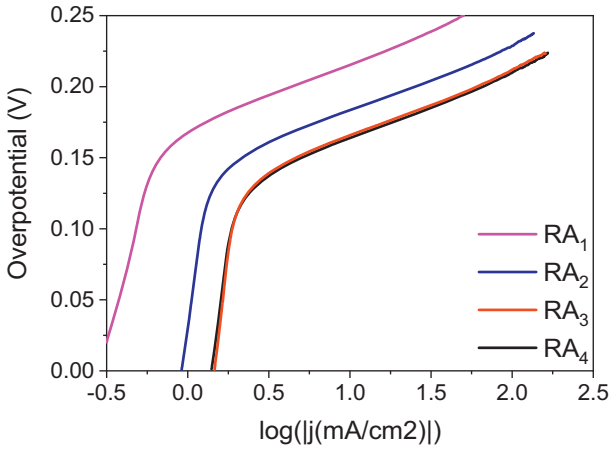

Fig. 8. Tafel plots of MoO_xS_y/CFPs (RA_1, RA_2, RA_3, and RA_4).

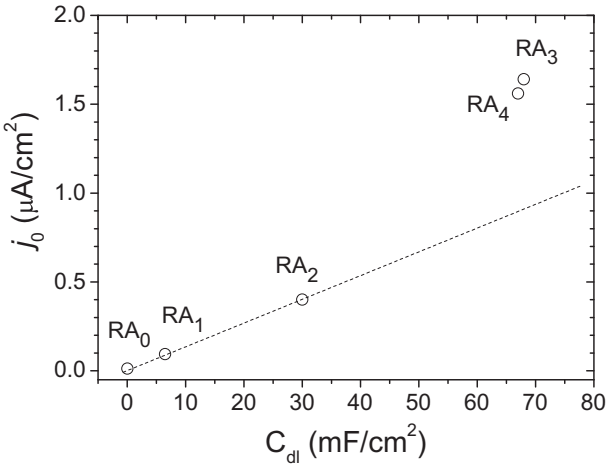

Fig. 9. Correlation between j_0 and C_{dl} in MoO_xS_y/CFP catalysts.

CFP catalysts, because the j_0 values are calculated by dividing the measured exchange current (i_0) by the geometric area (A_g) of the MoO_xS_y/CFP catalysts (i.e., $j_0 = i_0 / A_g$). It should be noted that the geometric area does not reflect surface roughness, porosity, and coverage of MoO_xS_y on the CFP.

Recently, Y. Li et al. reported that the exchange current density of catalysts is linearly proportional to the double layer capacitance for the catalysts with similar Tafel slopes [55]. As listed in Table 2, since the Tafel slopes of the MoO_xS_y/CFP catalysts are similar, it is expected that j_0 and C_{dl} are linearly correlated. Indeed, j_0 is linearly proportional to C_{dl} for the RA_0, RA_1, and RA_2 catalysts as shown in Fig. 9. This is because the coverage of MoO_xS_y on the CFP gradually increases from the partial (RA_0) to the complete (RA_2) coverage, as previously explained. However, the j_0 values of RA_3 (1.64 μA/cm^2) and RA_4 (1.56 μA/cm^2) catalysts severely deviate from the linear correlation in Fig. 9. The large deviation cannot be explained by an increase of coverage, because both catalysts have the complete coverage as the RA_2 catalyst. The exceptionally high HER activity of the RA_3 and RA_4 catalysts may be caused by enhancement of an intrinsic activity of active sites and/or an increase of electrical conductivity.

Although the ratios of monovalent (S_2^{2-}) and divalent (S^{2-}) sulfur anions are not severely varied with the concentration of reducing agent (Fig. 6b), the stoichiometric value (y) of sulfur in the MoO_xS_y catalysts significantly increases with the concentration of the reducing agent and then saturates at RA_3 and RA_4 catalysts (Fig. 2), indicating that the high y values contribute to the more excellent performance of RA_3 and RA_4 catalysts. Another possible reason for the high performance is that the oxygen-incorporated MoO_xS_y/CFP catalysts have high electrical conductivity which affects the exchange current density [56]. It was reported that the formation of MoO_3 species in the MoS_2-based catalysts impedes electron transport in the catalytic materials [57]. Since the presence of MoO_3 in the MoO_xS_y catalysts appears as a peak of Mo^{6+} in XPS spectra (Fig. 6(a)), it is revealed that the formation of the MoO_3 is relatively less pronounced in the RA_3 and RA_4 catalysts.

The Tafel slope (b), the slope of the linear region in the Tafel plot, is the overpotential required to increase the current density by one order of magnitude. Therefore, the catalyst with a lower Tafel slope is more advantageous for the electrocatalytic HER application than that with a higher value of Tafel slope. In terms of the Tafel slope, there is no significant difference among the MoO_xS_y/CFP catalysts as listed in Table 2. The Tafel slope depends on the mechanistic pathway. For the HER mechanism, three elementary reaction steps are known in acidic media:

discharge step (Volmer reaction):

$$H_3O^+ + e^- \rightarrow H_{ads} + H_2O$$

catalytic recombination step (Tafel reaction):

$$H_{ads} + H_{ads} \rightarrow H_2$$

electrochemical desorption step (Heyrovsky reaction):

$$H_{ads} + H_3O^+ + e^- \rightarrow H_2 + H_2O$$

For hydrogen evolution, the Volmer reaction should be followed by the Tafel or the Heyrovsky reaction. Therefore, there are two possible reaction pathways of Volmer-Tafel (VT) and Volmer-Heyrovsky (VH) pathways. Furthermore, these reaction pathways can be subdivided into four mechanisms ($\overline{V}T$, $V\overline{T}$, $\overline{V}H$ and $V\overline{H}$) depending on the position of rate-determining step (rds), where the upper bar denotes the rds. The theoretical value of the Tafel slope is determined by which step is the rds. According to the Butler-Volmer equation for HER based on the Langmuir adsorption model, the Tafel slopes of $\overline{V}T$, $V\overline{T}$, $\overline{V}H$ and $V\overline{H}$ mechanisms are 120, 30, 120 and 40 mV/dec, respectively. Considering the Tafel slopes of the MoO_xS_y/CFP catalysts (Table 2), the $V\overline{H}$ mechanism is the main pathway of HER on the MoO_xS_y/CFP catalysts.

In order to investigate the effect of oxygen incorporation to amorphous molybdenum sulfide catalysts, the MoO_xS_y/CFP catalysts were compared with amorphous oxygen-free MoS_x/CFPs previously reported by our group [58]. The MoS_x/CFP catalysts were prepared by a hydrothermal method using molybdic acid and thioacetamide. Unlike the MoO_xS_y/CFP catalysts which have clear vibration bands of Mo═O in the range of 800–960 cm^{-1} (Fig. 3), the MoS_x/CFP catalyst has no significant vibration band of Mo═O in Raman spectrum (Fig. S6), due to the absence of the incorporated oxygen atoms. The polarization curves of MoS_x/CFPs were depicted in dashed lines in Fig. 7, and the electrocatalytic characteristics were compared in Table 2. Even though the main mechanism on both O-incorporated and O-free catalysts is the same $V\overline{H}$ mechanism as revealed in the Tafel slopes, the MoO_xS_y catalysts exhibit much more excellent HER performance than the oxygen-free MoS_x/CFPs except for the RA_0 and RA_1 in which the MoO_xS_y catalyst does not completely cover the CFP substrate.

The most significant difference in chemical states of O-incorporated and O-free catalysts is the oxidation states of molybdenum. The oxidation state of Mo atoms in the O-free MoS_x/CFPs is mainly Mo^{4+} ion [58]. However, the tetravalent state (Mo^{4+}) of Mo atoms in the MoO_xS_y catalysts is mixed with pentavalent (Mo^{5+}) and hexavalent (Mo^{6+}) states as shown in Fig. 6(a). Since the oxidation state of Mo atoms in MoS_x (x = 2–3) is generally tetravalent (Mo^{4+}) [59], the presence of Mo^{5+} and Mo^{6+} states in our MoO_xS_y catalysts is intriguing. In several reports for O-incorporated molybdenum sulfide [42,45–47], the oxidation states of Mo^{5+} and Mo^{6+} did not appear in oxygen-doped MoO_xS_y catalysts with a low content of oxygen [42,46]. However, when the content of the incorporated oxygen is considerably high as in our MoO_xS_y catalysts, both Mo^{5+} and Mo^{6+} states were found in the MoO_xS_y catalysts [45,47].

It is believed that the positive effect of oxygen incorporation on the HER is not only attributed to higher electrical conductivity but also related to the presence of the Mo^{5+} state [42,44–47]. Note that the presence of MoO_3, of which molybdenum atoms have the Mo^{6+} state, impedes electron transport in the MoS_2-based catalysts due to its insulating property [57]. Recently, Tran et al. reported that the Mo^{5+} plays a role of additional active sites in the course of the catalytic pathway [30]. As shown in Fig. 6(a), the ratio of Mo^{5+} to the total molybdenum ions in the MoO_xS_y catalysts is approximately 30%, implying that a considerable amount of molybdenum ions of MoO_xS_y is catalytically active for HER. Furthermore, unlike the insulating property of MoO_3 [57], the non-stoichiometric MoO_{3-x} with Mo^{5+} and oxygen vacancies is electrically conducting [60]. Therefore, the presence of the Mo^{5+} state also contributes to the improvement of electrical conductivity in the MoO_xS_y catalysts [61].

Stability is a practical concern for the long-term operation of HER catalysts. The stability of the MoO_xS_y/CFP catalysts (RA_3 and RA_4) was

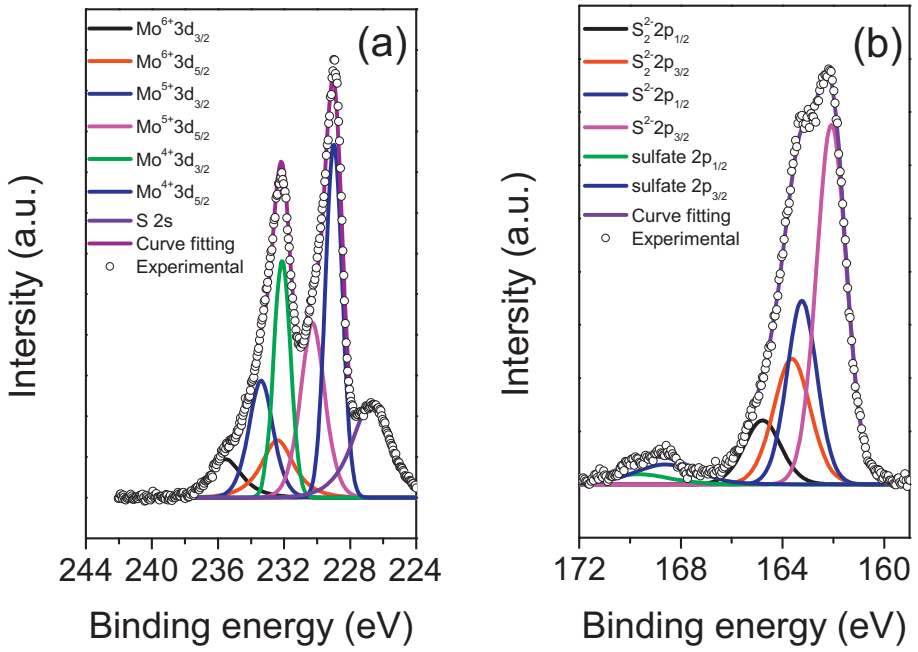

Fig. 10. XPS spectra of Mo 3d (a) and S 2p (b) core electrons of the MoO_xS_y/CFP catalyst (RA_3) after the stability test for 1000 CV cycles.

investigated by repeating a cyclic potential scan in the range from +0.1 to −0.4 V vs RHE with a scan rate of 5 mV/s. Comparing the polarization curves before and after repeating the 1000 CV cycles, there was no significant degradation of the cathodic current density as shown in Fig. S7. In order to confirm whether the chemical state of each Mo and S ion was changed after the stability test, the representative catalyst of RA_3, which had experienced 1000 CV cycles, was analyzed by XPS (Fig. 10), and the ratios of each ion were listed in Table S2. As expected from the stability test, there is no noticeable change in the ionic ratios. For example, the ratio of Mo^{5+} to the total molybdenum ions is 0.33 for the as-prepared catalyst and 0.35 after the stability test. It reveals that the Mo^{5+} ion of MoO_xS_y catalysts may continue to enhance the catalytic activity for the long-term evolution of hydrogen.

4. Conclusion

In order to investigate the effect of oxygen incorporation on the electrocatalytic activity of amorphous molybdenum sulfide (MoS_x) catalysts, the relation of chemical states and HER performance of catalysts were studied with the oxygen-incorporated MoO_xS_y catalysts. Comparing to the oxygen-free MoS_x/CFPs, the MoO_xS_y/CFP catalysts exhibit more excellent HER performance possibly due to the presence of Mo^{5+} species which provides additional active sites and improves electrical conductivity. Although the oxidation state of Mo^{5+} can be formed by incorporating oxygen atoms to the MoS_x catalysts, the level of the oxygen incorporation should be adjusted to suppress the excessive formation of Mo^{6+} state of electrically insulating MoO_3 in the catalyst.

Acknowledgements

This work was supported by Konkuk University in 2015.

Appendix A. Supplementary data

Supplementary data to this article can be found online at https://doi.org/10.1016/j.apsusc.2019.05.188.

References

[1] I. Roger, M.A. Shipman, M.D. Symes, Earth-abundant catalysts for electrochemical and photoelectrochemical water splitting, Nat. Rev. Chem. 1 (2017).
[2] Y. Yan, B. Xia, Z. Xu, X. Wang, Recent development of molybdenum sulfides as advanced electrocatalysts for hydrogen evolution reaction, ACS Catal. 4 (2014) 1693–1705.
[3] M. Zeng, Y. Li, Recent advances in heterogeneous electrocatalysts for the hydrogen evolution reaction, J. Mater. Chem. A 3 (2015) 14942–14962.
[4] Y. Shi, B. Zhang, Recent advances in transition metal phosphide nanomaterials: synthesis and applications in hydrogen evolution reaction, Chem. Soc. Rev. 45 (2016) 1529–1541.
[5] W.F. Chen, J.T. Muckerman, E. Fujita, Recent developments in transition metal carbides and nitrides as hydrogen evolution electrocatalysts, Chem. Commun. (Camb.) 49 (2013) 8896–8909.
[6] X. Zhang, C. Shi, B. Chen, A.N. Kuhn, D. Ma, H. Yang, Progress in hydrogen production over transition metal carbide catalysts: challenges and opportunities, Curr. Opin. Chem. Eng. 20 (2018) 68–77.
[7] T.F. Jaramillo, K.P. Jorgensen, J. Bonde, J.H. Nielsen, S. Horch, I. Chorkendorff, Identification of active edge sites for electrochemical H_2 evolution from MoS_2 nanocatalysts, Science 317 (2007) 100–102.
[8] D. Kong, H. Wang, J.J. Cha, M. Pasta, K.J. Koski, J. Yao, Y. Cui, Synthesis of MoS_2 and $MoSe_2$ films with vertically aligned layers, Nano Lett. 13 (2013) 1341–1347.
[9] H. Wang, Z. Lu, S. Xu, D. Kong, J.J. Cha, G. Zheng, P.C. Hsu, K. Yan, D. Bradshaw, F.B. Prinz, Y. Cui, Electrochemical tuning of vertically aligned MoS_2 nanofilms and its application in improving hydrogen evolution reaction, Proc. Natl. Acad. Sci. U. S. A. 110 (2013) 19701–19706.
[10] L. Yang, H. Hong, Q. Fu, Y. Huang, J. Zhang, X. Cui, Z. Fan, K. Liu, B. Xiang, Single-crystal atomic-layered molybdenum disulfide nanobelts with high surface activity, ACS Nano 9 (2015) 6478–6483.
[11] J. Xie, H. Zhang, S. Li, R. Wang, X. Sun, M. Zhou, J. Zhou, X.W. Lou, Y. Xie, Defect-rich MoS_2 ultrathin nanosheets with additional active edge sites for enhanced electrocatalytic hydrogen evolution, Adv. Mater. 25 (2013) 5807–5813.
[12] S.H. Lin, J.L. Kuo, Activating and tuning basal planes of MoO_2, MoS_2, and $MoSe_2$ for hydrogen evolution reaction, Phys. Chem. Chem. Phys. 17 (2015) 29305–29310.
[13] G. Li, D. Zhang, Q. Qiao, Y. Yu, D. Peterson, A. Zafar, R. Kumar, S. Curtarolo, F. Hunte, S. Shannon, Y. Zhu, W. Yang, L. Cao, All the catalytic active sites of MoS_2 for hydrogen evolution, J. Am. Chem. Soc. 138 (2016) 16632–16638.
[14] H. Li, M. Du, M.J. Mleczko, A.L. Koh, Y. Nishi, E. Pop, A.J. Bard, X. Zheng, Kinetic study of hydrogen evolution reaction over strained MoS_2 with sulfur vacancies using scanning electrochemical microscopy, J. Am. Chem. Soc. 138 (2016) 5123–5129.
[15] H. Li, C. Tsai, A.L. Koh, L. Cai, A.W. Contryman, A.H. Fragapane, J. Zhao, H.S. Han, H.C. Manoharan, F. Abild-Pedersen, J.K. Norskov, X. Zheng, Activating and optimizing MoS_2 basal planes for hydrogen evolution through the formation of strained sulphur vacancies, Nat. Mater. 15 (2016) 48–53.
[16] L. Lin, N. Miao, Y. Wen, S. Zhang, P. Ghosez, Z. Sun, D.A. Allwood, Sulfur-depleted monolayered molybdenum disulfide nanocrystals for superelectrochemical hydrogen evolution reaction, ACS Nano 10 (2016) 8929–8937.
[17] Y. Ouyang, C. Ling, Q. Chen, Z. Wang, L. Shi, J. Wang, Activating inert basal planes of MoS_2 for hydrogen evolution reaction through the formation of different intrinsic

defects, Chem. Mater. 28 (2016) 4390–4396.
[18] G. Ye, Y. Gong, J. Lin, B. Li, Y. He, S.T. Pantelides, W. Zhou, R. Vajtai, P.M. Ajayan, Defects engineered monolayer MoS_2 for improved hydrogen evolution reaction, Nano Lett. 16 (2016) 1097–1103.
[19] C. Tsai, H. Li, S. Park, J. Park, H.S. Han, J.K. Norskov, X. Zheng, F. Abild-Pedersen, Electrochemical generation of sulfur vacancies in the basal plane of MoS_2 for hydrogen evolution, Nat. Commun. 8 (2017) 15113.
[20] J. Deng, H. Li, J. Xiao, Y. Tu, D. Deng, H. Yang, H. Tian, J. Li, P. Ren, X. Bao, Triggering the electrocatalytic hydrogen evolution activity of the inert two-dimensional MoS_2 surface via single-atom metal doping, Energy Environ. Sci. 8 (2015) 1594–1601.
[21] G. Gao, Q. Sun, A. Du, Activating catalytic inert basal plane of molybdenum disulfide to optimize hydrogen evolution activity via defect doping and strain engineering, J. Phys. Chem. C 120 (2016) 16761–16766.
[22] D. Merki, S. Fierro, H. Vrubel, X. Hu, Amorphous molybdenum sulfide films as catalysts for electrochemical hydrogen production in water, Chem. Sci. 2 (2011) 1262–1267.
[23] J.D. Benck, Z. Chen, L.Y. Kuritzky, A.J. Forman, T.F. Jaramillo, Amorphous molybdenum sulfide catalysts for electrochemical hydrogen production: insights into the origin of their catalytic activity, ACS Catal. 2 (2012) 1916–1923.
[24] D. Merki, H. Vrubel, L. Rovelli, S. Fierro, X. Hu, Fe, Co, and Ni ions promote the catalytic activity of amorphous molybdenum sulfide films for hydrogen evolution, Chem. Sci. 3 (2012).
[25] H. Vrubel, X. Hu, Growth and activation of an amorphous molybdenum sulfide hydrogen evolving catalyst, ACS Catal. 3 (2013) 2002–2011.
[26] H.G.S. Casalongue, J.D. Benck, C. Tsai, R.K.B. Karlsson, S. Kaya, M.L. Ng, L.G.M. Pettersson, F. Abild-Pedersen, J.K. Nørskov, H. Ogasawara, T.F. Jaramillo, A. Nilsson, Operando characterization of an amorphous molybdenum sulfide nanoparticle catalyst during the hydrogen evolution reaction, J. Phys. Chem. C 118 (2014) 29252–29259.
[27] B. Lassalle-Kaiser, D. Merki, H. Vrubel, S. Gul, V.K. Yachandra, X. Hu, J. Yano, Evidence from in situ X-ray absorption spectroscopy for the involvement of terminal disulfide in the reduction of protons by an amorphous molybdenum sulfide electrocatalyst, J. Am. Chem. Soc. 137 (2015) 314–321.
[28] Y. Deng, L.R.L. Ting, P.H.L. Neo, Y.-J. Zhang, A.A. Peterson, B.S. Yeo, Operando Raman spectroscopy of amorphous molybdenum sulfide (MoS_x) during the electrochemical hydrogen evolution reaction: identification of sulfur atoms as catalytically active sites for H^+ reduction, ACS Catal. 6 (2016) 7790–7798.
[29] L.R.L. Ting, Y. Deng, L. Ma, Y.-J. Zhang, A.A. Peterson, B.S. Yeo, Catalytic activities of sulfur atoms in amorphous molybdenum sulfide for the electrochemical hydrogen evolution reaction, ACS Catal. 6 (2016) 861–867.
[30] P.D. Tran, T.V. Tran, M. Orio, S. Torelli, Q.D. Truong, K. Nayuki, Y. Sasaki, S.Y. Chiam, R. Yi, I. Honma, J. Barber, V. Artero, Coordination polymer structure and revisited hydrogen evolution catalytic mechanism for amorphous molybdenum sulfide, Nat. Mater. 15 (2016) 640–646.
[31] H. Vrubel, T. Moehl, M. Grätzel, X. Hu, Revealing and accelerating slow electron transport in amorphous molybdenum sulphide particles for hydrogen evolution reaction, Chem. Commun. 49 (2013).
[32] P. Luo, F. Zhuge, Q. Zhang, Y. Chen, L. Lv, Y. Huang, H. Li, T. Zhai, Doping engineering and functionalization of two-dimensional metal chalcogenides, Nanoscale Horiz. 4 (2019) 26–51.
[33] J. Pan, C. Song, X. Wang, X. Yuan, Y. Fang, C. Guo, W. Zhao, F. Huang, Intermediate bands of MoS_2 enabled by Co doping for enhanced hydrogen evolution, Inorg. Chem. Front. 4 (2017) 1895–1899.
[34] H. Wang, C. Tsai, D. Kong, K. Chan, F. Abild-Pedersen, J.K. Nørskov, Y. Cui, Transition-metal doped edge sites in vertically aligned MoS_2 catalysts for enhanced hydrogen evolution, Nano Res. 8 (2015) 566–575.
[35] R. Li, L. Yang, T. Xiong, Y. Wu, L. Cao, D. Yuan, W. Zhou, Nitrogen doped MoS_2 nanosheets synthesized via a low-temperature process as electrocatalysts with enhanced activity for hydrogen evolution reaction, J. Power Sources 356 (2017) 133–139.
[36] X. Zhang, F. Meng, S. Mao, Q. Ding, M.J. Shearer, M.S. Faber, J. Chen, R.J. Hamers, S. Jin, Amorphous MoS_xCl_y electrocatalyst supported by vertical graphene for efficient electrochemical and photoelectrochemical hydrogen generation, Energy Environ. Sci. 8 (2015) 862–868.
[37] T.H.M. Lau, X. Lu, J. Kulhavy, S. Wu, L. Lu, T.S. Wu, R. Kato, J.S. Foord, Y.L. Soo, K. Suenaga, S.C.E. Tsang, Transition metal atom doping of the basal plane of MoS_2 monolayer nanosheets for electrochemical hydrogen evolution, Chem. Sci. 9 (2018) 4769–4776.
[38] P. Liu, J. Zhu, J. Zhang, K. Tao, D. Gao, P. Xi, Active basal plane catalytic activity and conductivity in Zn doped MoS_2 nanosheets for efficient hydrogen evolution, Electrochim. Acta 260 (2018) 24–30.
[39] X. Sun, J. Dai, Y. Guo, C. Wu, F. Hu, J. Zhao, X. Zeng, Y. Xie, Semimetallic molybdenum disulfide ultrathin nanosheets as an efficient electrocatalyst for hydrogen evolution, Nanoscale 6 (2014) 8359–8367.
[40] L. Wu, X. Xu, Y. Zhao, K. Zhang, Y. Sun, T. Wang, Y. Wang, W. Zhong, Y. Du, Mn doped MoS_2/reduced graphene oxide hybrid for enhanced hydrogen evolution, Appl. Surf. Sci. 425 (2017) 470–477.
[41] X. Ren, Q. Ma, H. Fan, L. Pang, Y. Zhang, Y. Yao, X. Ren, S.F. Liu, A Se-doped MoS_2 nanosheet for improved hydrogen evolution reaction, Chem. Commun. (Camb.) 51 (2015) 15997–16000.
[42] J. Xie, J. Zhang, S. Li, F. Grote, X. Zhang, H. Zhang, R. Wang, Y. Lei, B. Pan, Y. Xie, Controllable disorder engineering in oxygen-incorporated MoS_2 ultrathin nanosheets for efficient hydrogen evolution, J. Am. Chem. Soc. 135 (2013) 17881–17888.
[43] X.-Q. Bao, D.Y. Petrovykh, P. Alpuim, D.G. Stroppa, N. Guldris, H. Fonseca, M. Costa, J. Gaspar, C. Jin, L. Liu, Amorphous oxygen-rich molybdenum oxysulfide decorated p-type silicon microwire arrays for efficient photoelectrochemical water reduction, Nano Energy 16 (2015) 130–142.
[44] J. Guo, F. Li, Y. Sun, X. Zhang, L. Tang, Oxygen-incorporated MoS_2 ultrathin nanosheets grown on graphene for efficient electrochemical hydrogen evolution, J. Power Sources 291 (2015) 195–200.
[45] A. Liu, L. Zhao, J. Zhang, L. Lin, H. Wu, Solvent-assisted oxygen incorporation of vertically aligned MoS_2 ultrathin nanosheets decorated on reduced graphene oxide for improved electrocatalytic hydrogen evolution, ACS Appl. Mater. Interfaces 8 (2016) 25210–25218.
[46] J. Xie, J. Xin, G. Cui, X. Zhang, L. Zhou, Y. Wang, W. Liu, C. Wang, M. Ning, X. Xia, Y. Zhao, B. Tang, Vertically aligned oxygen-doped molybdenum disulfide nanosheets grown on carbon cloth realizing robust hydrogen evolution reaction, Inorg. Chem. Front. 3 (2016) 1160–1166.
[47] J. Zhou, G. Fang, A. Pan, S. Liang, Oxygen-incorporated MoS_2 nanosheets with expanded interlayers for hydrogen evolution reaction and pseudocapacitor applications, ACS Appl. Mater. Interfaces 8 (2016) 33681–33689.
[48] L. Bian, W. Gao, J. Sun, M. Han, F. Li, Z. Gao, L. Shu, N. Han, Z.-x. Yang, A. Song, Y. Qu, J.C. Ho, Phosphorus-doped MoS_2 nanosheets supported on carbon cloths as efficient hydrogen-generation electrocatalysts, ChemCatChem 10 (2018) 1571–1577.
[49] W. Shi, Z. Wang, Effect of oxygen doping on the hydrogen evolution reaction in MoS_2 monolayer, J. Taiwan Inst. Chem. Eng. 82 (2018) 163–168.
[50] S.K. Chung, Mechanism of sodium dithionite reduction of aldehydes and ketones, J. Org. Chem. 46 (1981) 5457–5458.
[51] K.L. Williamson, Reduction of indigo: sodium hydrosulfite as a reducing agent, J. Chem. Educ. 66 (1989).
[52] C.V. Krishnan, M. Garnett, B. Hsiao, a.B. Chu, Electrochemical measurements of isopolyoxomolybdates: 1. pH dependent behavior of sodium molybdate, Int. J. Electrochem. Sci. 2 (2007) 29–51.
[53] P. Pramanik, S. Bhattacharya, Deposition of molybdenum chalcogenide thin films by the chemical deposition technique and the effect of bath parameters on these thin films, Mater. Res. Bull. 25 (1990) 15–23.
[54] L. Benoist, D. Gonbeau, G. Pfisterguillouzo, E. Schmidt, G. Meunier, A. Levasseur, X-ray photoelectron-spectroscopy characterization of amorphous molybdenum oxysulfide thin-films, Thin Solid Films 258 (1995) 110–114.
[55] Y.P. Li, Y.F. Yu, Y.F. Huang, R.A. Nielsen, W.A. Goddard, Y. Li, L.Y. Cao, Engineering the composition and crystallinity of molybdenum sulfide for high-performance electrocatalytic hydrogen evolution, ACS Catal. 5 (2015) 448–455.
[56] Y. Yu, S.Y. Huang, Y. Li, S.N. Steinmann, W. Yang, L. Cao, Layer-dependent electrocatalysis of MoS_2 for hydrogen evolution, Nano Lett. 14 (2014) 553–558.
[57] C. Zhang, L. Jiang, Y. Zhang, J. Hu, M.K.H. Leung, Janus effect of O_2 plasma modification on the electrocatalytic hydrogen evolution reaction of MoS_2, J. Catal. 361 (2018) 384–392.
[58] R. Bose, S.K. Balasingam, S. Shin, Z. Jin, D.H. Kwon, Y. Jun, Y.S. Min, Importance of hydrophilic pretreatment in the hydrothermal growth of amorphous molybdenum sulfide for hydrogen evolution catalysis, Langmuir 31 (2015) 5220–5227.
[59] T. Weber, J.C. Muijsers, J.W. Niemantsverdriet, Structure of amorphous Mos_3, J. Phys. Chem. 99 (1995) 9194–9200.
[60] M.T. Greiner, L. Chai, M.G. Helander, W.-M. Tang, Z.-H. Lu, Transition metal oxide work functions: the influence of cation oxidation state and oxygen vacancies, Adv. Funct. Mater. 22 (2012) 4557–4568.
[61] E. Schmidt, C. Sourisseau, G. Meunier, A. Levasseur, Amorphous molybdenum oxysulfide thin films and their physical characterization, Thin Solid Films 260 (1995) 21–25.

Effect of Oxygen Incorporation in Amorphous Molybdenum Sulfide on Electrochemical Hydrogen Evolution

Seokhee Shin, Zhenyu Jin, So-Yeon Ham, Suhyun Lee, Da-Som Shin and Yo-Sep Min*

Department of Chemical Engineering, Konkuk University, 120 Neungdong-Ro, Gwangjin-Gu, Seoul 05029, Korea

*Corresponding Author

Email address: ysmin@konkuk.ac.kr (Y. S. Min)

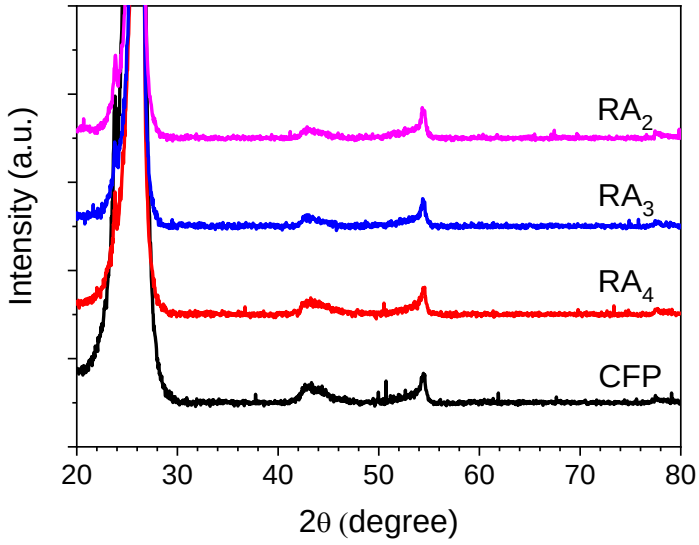

Figure S1. XRD patterns of MoO_xS_y/CFPs (R_2, R_3 and R_4) and a bare CFP.

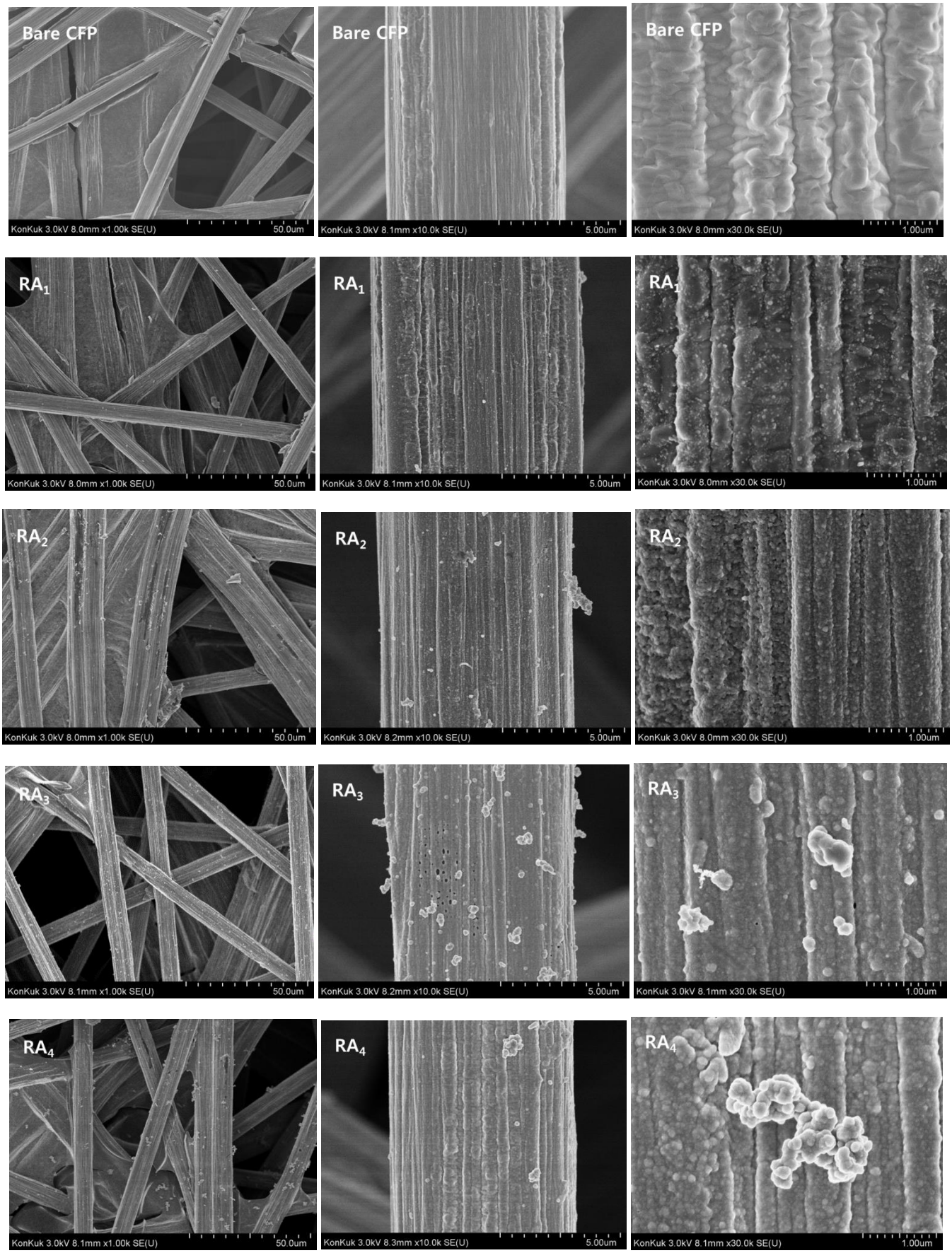

Figure S2. FE-SEM images of a bare CFP and MoO_xS_y/CFP catalysts.

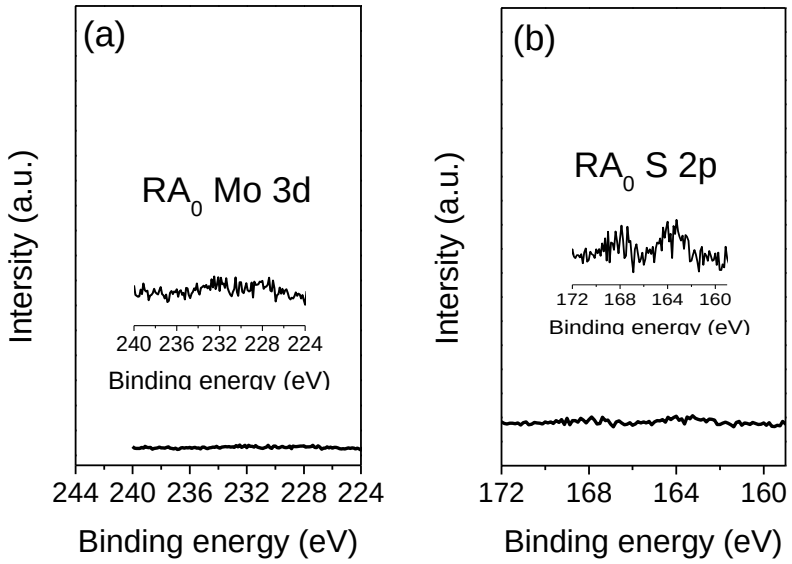

Figure S3. XPS spectra of Mo 3d and S 2p core electrons of catalyst RA_0 prepared without using NaS_2O_4. Insets were enlarged 10 times, because the intensity of each spectrum is low and noisy when plotted with the same scale as shown in Fig. 4 and Fig. 5.

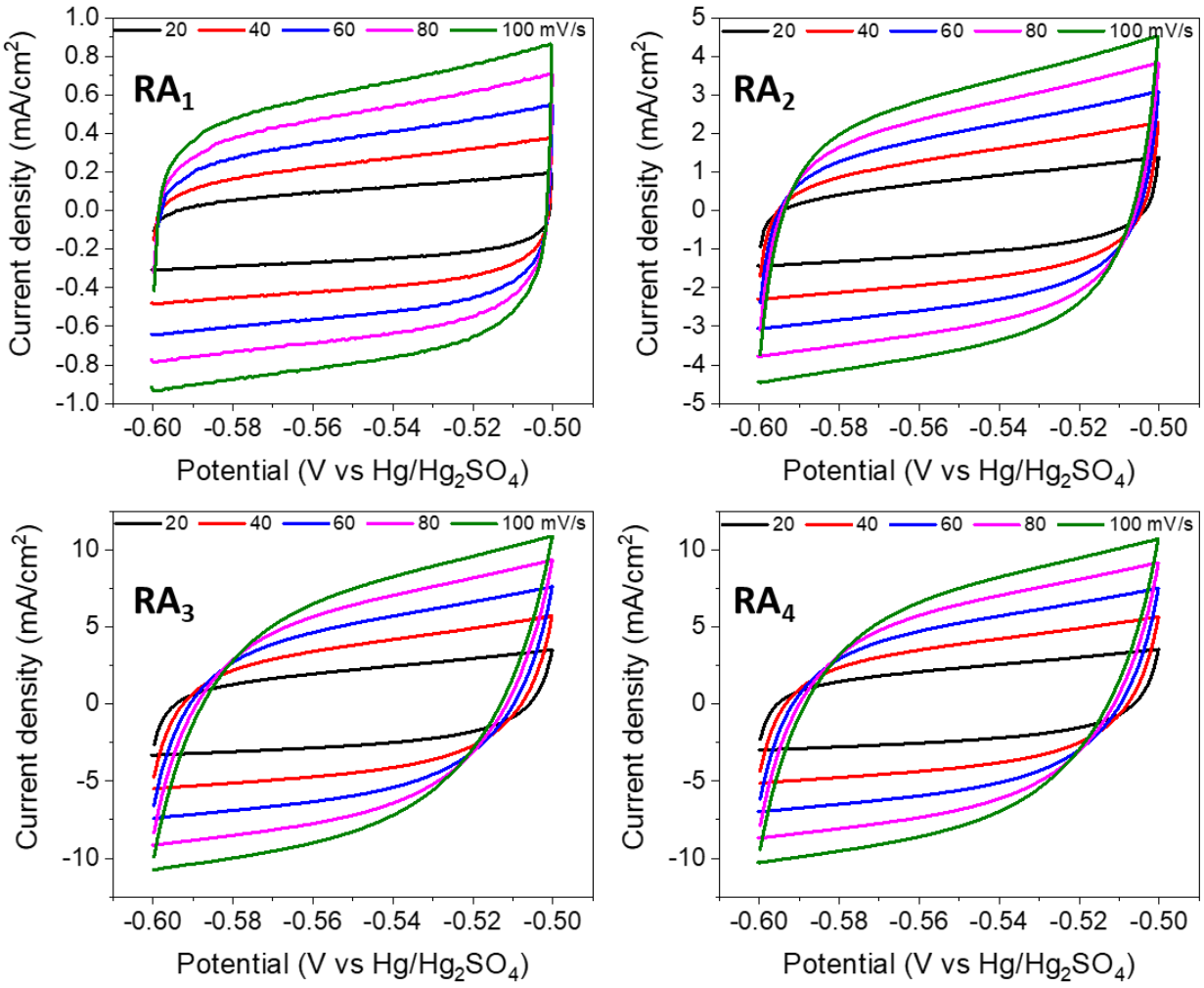

Figure S4. Cyclic voltammograms of MoO_xS_y catalysts to measure the electric double layer capacitance (C_{dl}).

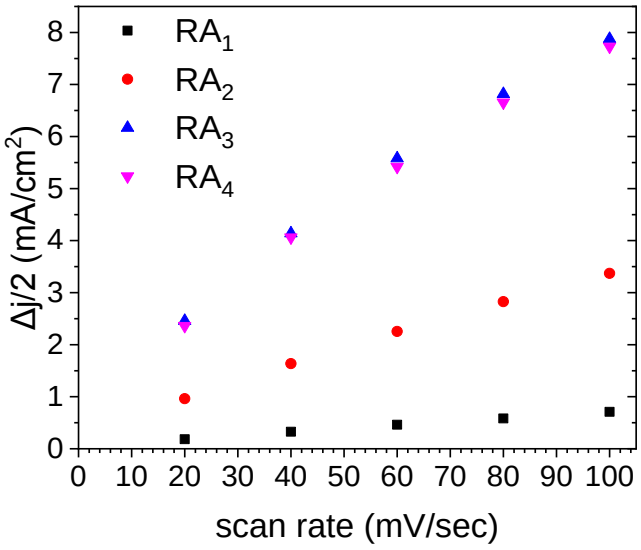

Figure S5. Plots showing the extraction of the double layer capacitance (C_{dl}) of MoO_xS_y catalysts.

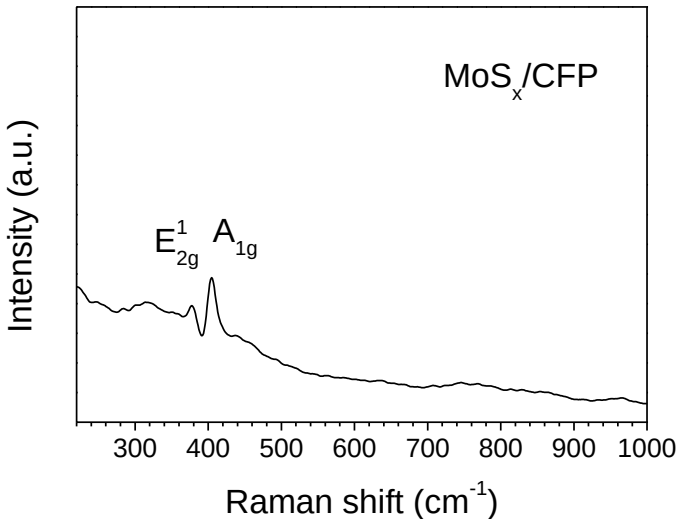

Figure S6. Representative Raman spectrum of oxygen-free MoS_x/CFP prepared by a hydrothermal method using molybdic acid and thioacetamide in our previous work (Ref. 58).

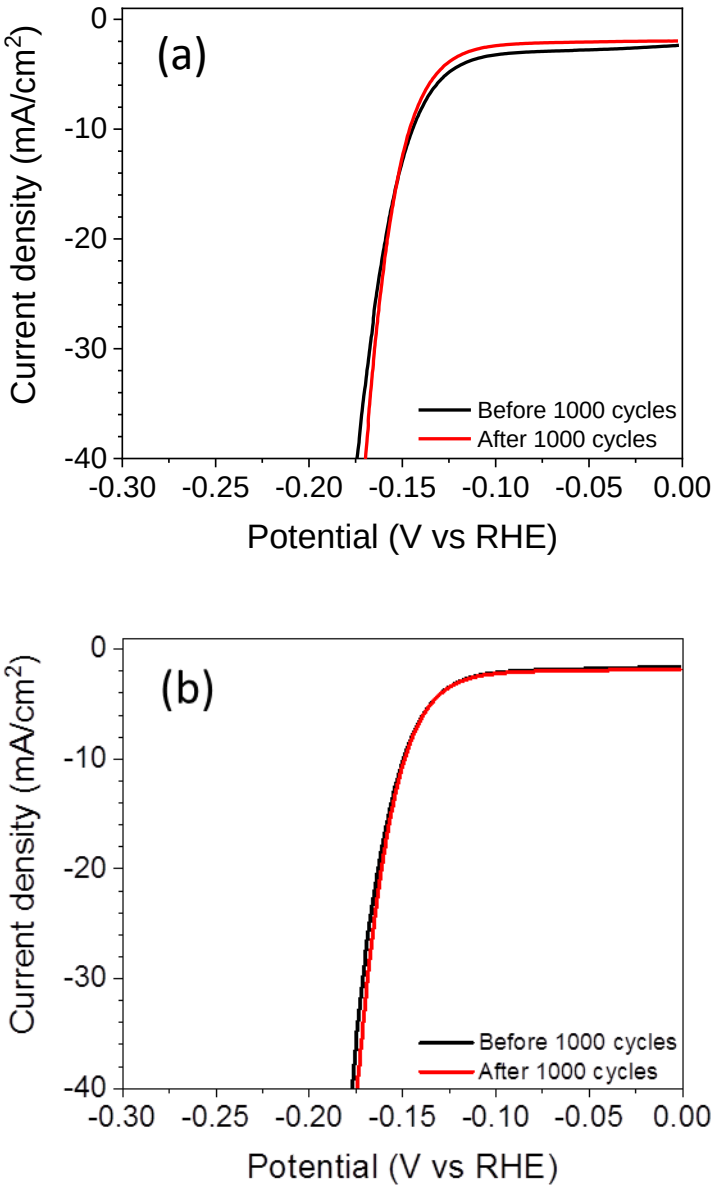

Figure S7. Polarization curves of MoO_xS_y/CFP catalysts before and after repeating 1000 CV cycles between +0.1 and −0.4 V vs RHE: (a) RA_3 and (b) RA_4.

Table S1. Deconvoluted XPS data for MoO_xS_y catalysts.

Samples	Mo^{4+} (eV)		Mo^{5+} (eV)		Mo^{6+} (eV)		S^{2-} (eV)		S_2^{2-} (eV)		S^{6+} (eV)	
	$3d_{5/2}$	$3d_{3/2}$	$3d_{5/2}$	$3d_{3/2}$	$3d_{5/2}$	$3d_{3/2}$	$2p_{3/2}$	$2p_{1/2}$	$2p_{3/2}$	$2p_{1/2}$	$2p_{3/2}$	$2p_{1/2}$
RA_1	228.9	232.0	230.7	233.8	232.6	235.7	162.0	163.2	163.8	165.0	168.7	169.9
RA_2	229.3	232.4	230.8	234.0	232.6	235.7	161.9	163.1	163.3	164.5	168.3	169.5
RA3	229.3	232.4	230.6	233.8	232.3	235.5	161.9	163.1	163.4	164.6	168.3	169.4
RA_4	229.3	232.5	231.0	234.1	232.7	235.9	161.9	163.1	163.2	164.4	168.5	169.6

Table S2. Ratios of each ion in the representative MoO_xS_y/CFP (RA_3)

catalyst history	Mo ion ratio			S ion ratio		
	Mo^{4+}	Mo^{5+}	Mo^{6+}	S^{2-}	S_2^{2-}	S^{6+}
as-prepared	0.49	0.33	0.18	0.68	0.27	0.05
after 1000 cycles	0.48	0.35	0.17	0.65	0.28	0.08